Chemical Science

ROYAL SOCIETY OF CHEMISTRY

EDGE ARTICLE

View Article Online
View Journal | View Issue

Cite this: *Chem. Sci.*, 2021, **12**, 14484

All publication charges for this article have been paid for by the Royal Society of Chemistry

Elucidating the structure-dependent selectivity of CuZn towards methane and ethanol in CO_2 electroreduction using tailored Cu/ZnO precatalysts†

Seyedeh Behnaz Varandili,[a] Dragos Stoian,[a] Jan Vavra,[a] Kevin Rossi,[a] James R. Pankhurst,[a] Yannick T. Guntern,[a] Núria López[b] and Raffaella Buonsanti*[a]

Received 4th August 2021
Accepted 6th October 2021

DOI: 10.1039/d1sc04271h

rsc.li/chemical-science

Understanding the catalyst compositional and structural features that control selectivity is of uttermost importance to target desired products in chemical reactions. In this joint experimental–computational work, we leverage tailored Cu/ZnO precatalysts as a material platform to identify the intrinsic features of methane-producing and ethanol-producing CuZn catalysts in the electrochemical CO_2 reduction reaction (CO_2RR). Specifically, we find that Cu@ZnO nanocrystals, where a central Cu domain is decorated with ZnO domains, and ZnO@Cu nanocrystals, where a central ZnO domain is decorated with Cu domains, evolve into Cu@CuZn core@shell catalysts that are selective for methane (~52%) and ethanol (~39%), respectively. *Operando* X-ray absorption spectroscopy and various microscopy methods evidence that a higher degree of surface alloying along with a higher concentration of metallic Zn improve the ethanol selectivity. Density functional theory explains that the combination of electronic and tandem effects accounts for such selectivity. These findings mark a step ahead towards understanding structure–property relationships in bimetallic catalysts for the CO_2RR and their rational tuning to increase selectivity towards target products, especially alcohols.

Introduction

The electrochemical CO_2 reduction reaction (CO_2RR) has the potential to mitigate rising CO_2 levels while storing renewable energy in chemical bonds.[1] Among the different products, alcohols are highly desirable as they possess high energy density and ease of storage.[1] However, the progress toward obtaining them with high selectivity remains limited compared to that made in the production of gaseous hydrocarbon products.[2]

Copper is the only single metal capable of producing products beyond CO, including alcohols.[1,2] While this catalyst holds record efficiencies towards methane and ethylene, its lower selectivity toward ethanol is attributed to the higher energy barrier of ethanol formation with respect to ethylene, whose pathway shares common intermediates with the former.[1,2]

Tandem schemes and modification of the electronic properties of copper achieved by coupling it with a second element are promising strategies to improve its selectivity towards alcohols, particularly ethanol.[2–10] Most of the studies so far have focused on the composition dependence of the catalytic behaviour.[2–10] However, the sensitivity of the catalytic performance to the atomic distribution within bimetallic catalysts remains still underexplored.[2–10]

Among other systems, CuZn stands out because of two reasons. On one hand, this catalyst consists of two Earth abundant metals, which makes it particularly appealing. On the other hand, the conclusions of previous studies on its catalytic behaviour are controversial.[9–15] While high selectivity for ethanol was found in certain cases, preferential methane production was also reported, as well as selectivity towards CO.[9–15] Composition certainly plays an important role in directing selectivity, with a higher Zn content generally favouring CO;[13,16] yet other factors must come into play to justify the observed selectivity patterns towards methane or ethanol in similar compositional ranges.[9–15] For example, CuZn nanostructured catalysts were shown to facilitate the formation of ethanol at a Zn content between 10% and 30%.[9–12] Instead, CuZn nanoparticles with a similar Zn content were reported to favour selectivity toward methane.[15] Unfortunately, direct

[a]*Laboratory of Nanochemistry for Energy (LNCE), Institute of Chemical Sciences and Engineering, École Polytechnique Fédérale de Lausanne, CH-1950 Sion, Switzerland. E-mail: raffaella.buonsanti@epfl.ch*

[b]*Institute of Chemical Research of Catalonia (ICIQ), The Barcelona Institute of Science and Technology, 43007 Tarragona, Spain*

† Electronic supplementary information (ESI) available. See DOI: 10.1039/d1sc04271h

comparisons between these two systems and, similarly, in other examples, are impeded by the striking structural differences and size regime of the catalysts, one being nanostructured thin films with agglomerated particles of sizes 100 nm to 1 μm, and the other consisting of 5 nm nanoparticles. Nevertheless, understanding the catalyst features which are optimal to direct the reaction pathway towards target products is of uttermost importance to move towards rational catalyst design, which is particularly urgent in the CO_2RR.

In this work, we employ tailored Cu/ZnO precatalysts to link the composition and structure of CuZn catalysts to the promotion of ethanol *versus* methane. State-of-the-art material synthesis is coupled with operando X-ray absorption spectroscopy, various microscopy methods and theoretical calculations to find that the metal distribution plays a crucial role, together with the composition, in directing the selectivity of CuZn catalysts.

Results and discussion

Synthesis and characterization of the Cu/ZnO precatalysts

Cu/ZnO nanocrystals (NCs) were employed as precatalysts. They were synthesized *via* a previously developed seed-mediated approach to obtain tunable spatial configuration of Cu and ZnO domains within a single nano-object.[25,26] Two different sizes of ZnO NCs were used as seeds, namely 13 nm and 60 nm (Fig. S1†). The Cu : Zn atomic ratios were varied by adjusting the concentration of seeds and the amount of Cu precursor (Fig. S2†).

Fig. 1 displays the electron microscopy characterization of two representative Cu/ZnO NCs obtained with the smaller (Fig. 1a and b) and with the bigger (Fig. 1c and d) ZnO seeds, both with a Zn atomic content equal to 54%. The former are composed of a central 25 nm Cu domain decorated by ZnO domains, similar to previous results.[25] In the latter, each 60 nm ZnO seed is decorated by 25 nm Cu NCs. We will refer to these two types of Cu/ZnO NCs as Cu@ZnO and ZnO@Cu, respectively. The impact of the seed size on the final configuration of the Cu/ZnO NCs can be tentatively explained with strain accommodation arguments related to the high lattice mismatch between Cu and ZnO (Fig. S3†). Based on these arguments, we speculate that a higher misfit strain energy accumulates at the interfaces between the two domains in the ZnO@Cu NCs compared to the Cu@ZnO NCs. Additional characterization, including X-ray photoelectron spectroscopy (XPS) and X-ray diffraction (XRD), was performed to confirm the composition of the NCs and to rule out the possibility of a CuZn alloy in the as-synthesized NCs (Fig. S4†).

Characterization of the activated catalysts

In agreement with previous studies, we found that ZnO reduces to metallic Zn under CO_2RR conditions (Fig. S5†) and, concomitantly, the catalytic performance changes over time.[10,15] In order to decouple, or at least to minimize, the drastic effects of the structural changes on the catalytic behaviour, we opted for the introduction of a catalyst activation step, which involves

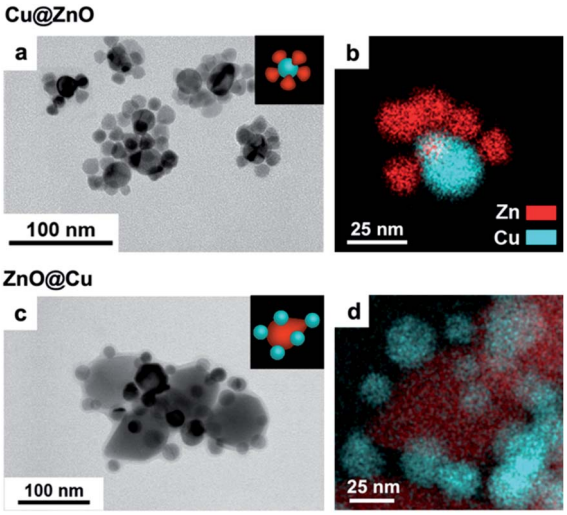

Fig. 1 (a and c) Representative low-resolution TEM and (b and d) STEM-EDXS elemental maps of the Cu@ZnO and ZnO@Cu precatalysts, synthesized by using ZnO NCs with a diameter of 13 nm and 60 nm as seeds, respectively.

the application of a cathodic potential of −1.1 V *vs.* RHE to the Cu/ZnO precatalysts. This potential was chosen to be close to the range in which the CO_2RR normally occurs for Cu-based nano catalysts.[6,26,27]

The activated catalysts were characterized by scanning transmission electron microscopy-energy dispersive X-ray spectroscopy (STEM-EDXS), X-ray photoelectron spectroscopy (XPS) and *operando* X-ray absorption near edge structure (XANES) measurements (Fig. 2). Fig. 2a and b report the STEM-EDXS elemental maps of the activated Cu@ZnO and ZnO@Cu NCs. Both systems evolve towards a core@shell structure, where a central Cu domain is surrounded by a few nanometer-thick Zn shell. The size of the Cu core remains the same as the precatalysts, which is around 25 nm, and regulates the size of the activated catalysts. The Zn shell appears slightly more uniform in the case of ZnO@Cu NCs (Fig. 2b). The XPS data were consistent with an increase of the Zn : Cu ratio on the surface of the activated catalysts, which was more evident for ZnO@Cu, in line with the higher uniformity of the shell (Fig. S6 and Table S1†). Some variation in the elemental distribution is noticeable in STEM-EDX; however no pure Cu or Zn particles were detected on the electrodes.

While it provides unique insight into the morphological and compositional evolution, electron microscopy is a local technique. Information on the composition at the ensemble level, such as that provided by XANES measurements, is needed for the interpretation of the catalytic properties. Fig. 2c compares the Zn K-edge of the XANES spectra for Cu@ZnO and ZnO@Cu before and after activation. The data for the as-synthesized samples evidence that Zn is initially fully oxidized while Cu is mostly in its metallic form. Upon activation, the ZnO component evolves towards its reduced form for both precatalysts (Fig. 2c). Furthermore, their final spectra suggest the presence of cationic Zn in the activated Cu@ZnO but not in the activated

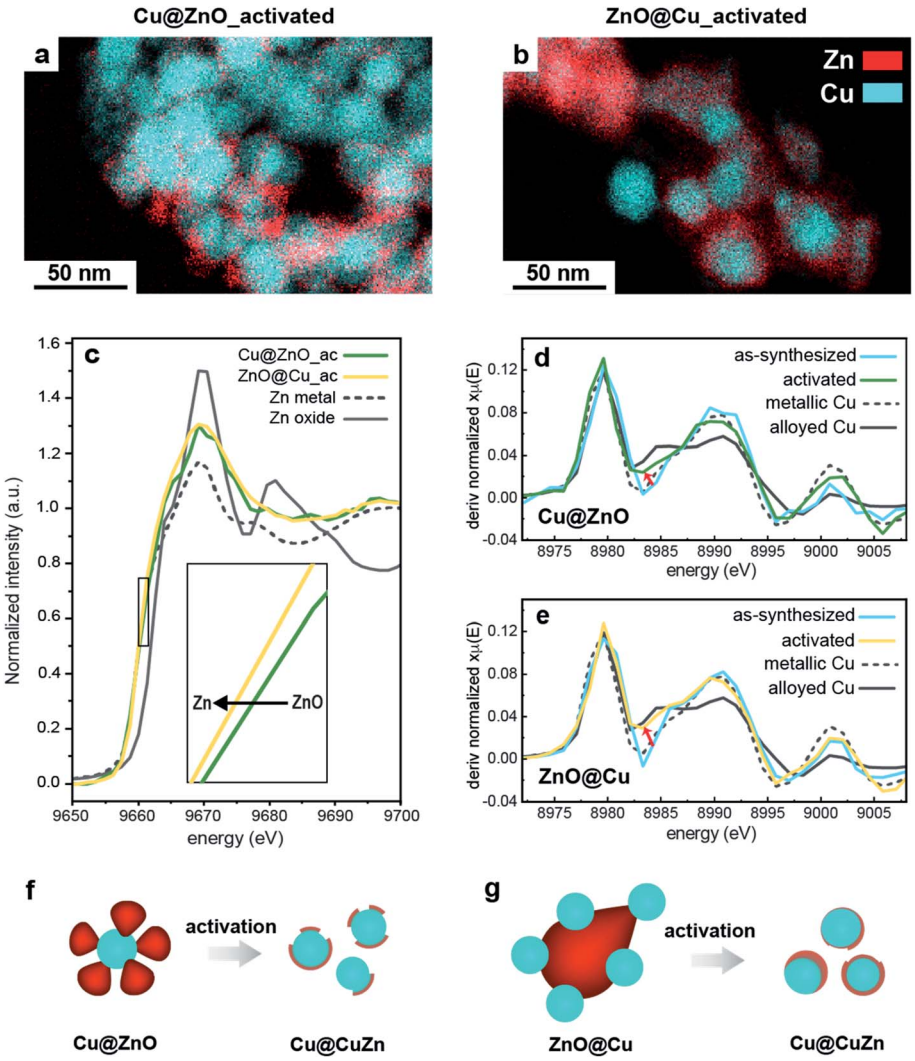

Fig. 2 (a and b) EDXS elemental maps of Cu@ZnO and ZnO@Cu after activation at −1.1 V_{RHE} for 1 hour. (c) Zn K-edge XANES spectra of ZnO@Cu and Cu@ZnO NCs after activation together with the spectra of reference Zn and ZnO particles. (d and e) First-order derivative of the Cu K-edge XANES spectra of the as-synthesized and activated samples. (f and g) Schematic of the morphological evolution of both NCs during activation.

ZnO@Cu NCs. No strikingly evident changes were observed for the Cu K-edge spectra upon activation.

In order to investigate the possibility of alloying between Cu and Zn, the first-derivative XANES spectra of the samples before and after activation were plotted along with Cu and Zn reference materials in metallic, alloyed and oxide forms (Fig. 2d, e and S7†). The data of the Cu K-edge in both activated catalysts are consistent with the partial alloying of Cu with Zn (Fig. 2d and e). This is particularly evident in ZnO@Cu (Fig. 2e), where the spectrum of the as-synthesized sample is similar to that of metallic Cu (note the spectra around 8982–8985 eV), while the final spectrum after activation clearly overlaps with that of the alloyed CuZn reference (the trend of changes is shown by a black arrow). As for the Zn K-edge, the changes in the line profiles of all the samples are consistent with metallic Zn and some degree of alloyed Zn (Fig. S7†).

Finally, elemental analysis indicated that a small fraction of Zn leaches into the electrolyte for both precatalysts, which suggests that some dissolution/reprecipitation processes might occur during the activation. The extent of Zn leaching during activation is similar in the two NCs. Indeed, the pre-catalysts with initial 54% Zn enter the course of the CO_2RR with a Zn atomic percentage of ~48%.

To summarize, we found that the activation of Cu@ZnO and ZnO@Cu yields Cu@CuZn core@shell structures (Fig. 2f and g). The Cu@ZnO-derived catalysts possess a less uniform shell and some residual cationic Zn species. The ZnO@Cu-derived catalysts exhibit a more uniform shell and the Zn domain is in a completely metallic state. The more drastic reconstruction of the ZnO@Cu NCs, which undergo a complete inversion of the core and the shell, can be speculatively attributed to their highly strained interfaces. Interestingly, a physical mixture of Cu and ZnO NCs does not evolve into the same type of structure (Fig. S6, S8 and Table S1†). The finding that the interface between Cu and ZnO in the precatalysts plays an important role in the reconstruction is certainly interesting and deserves further

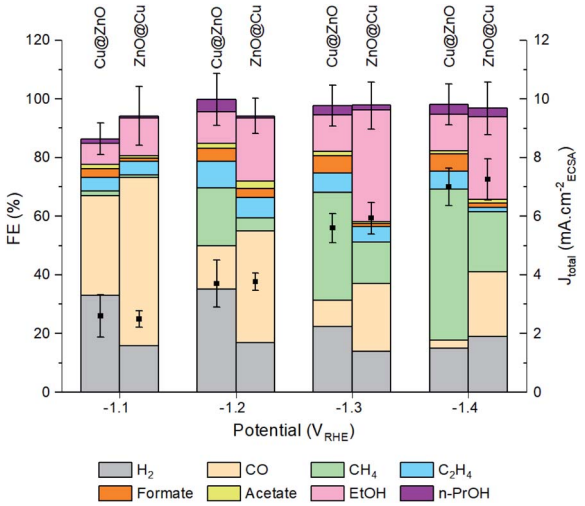

Fig. 3 FEs for different products and CO_2RR partial current densities at variable potentials for ZnO@Cu and Cu@ZnO, pre-activated at −1.1 V_{RHE} (20 μg drop-cast on 1 cm^2 glassy carbon). The error bars for total FE and J_{total} correspond to the standard deviation from three independent measurements.

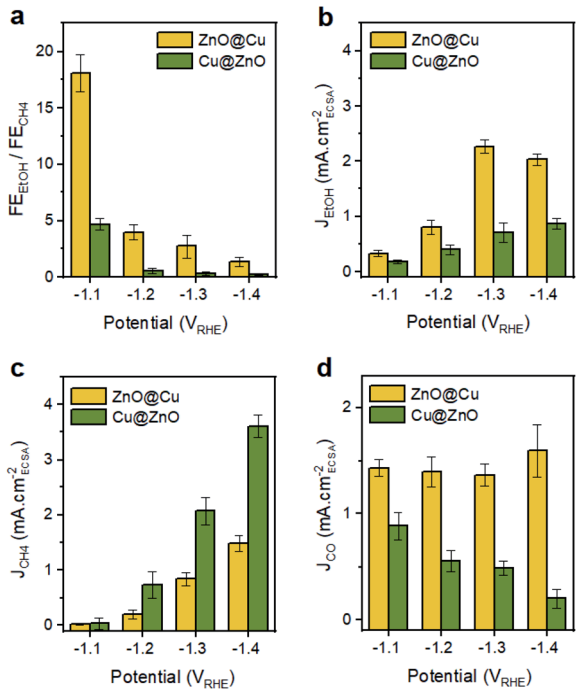

Fig. 4 (a) FE_{EtOH}/FE_{CH_4} and (b–d) ECSA-normalized partial current densities for EtOH, CH_4 and CO over activated ZnO@Cu and Cu@ZnO NCs.

investigation. However, dedicated studies, which combine identical location or *in situ* microscopy studies with sensitive analytical techniques, are needed to further understand this phenomenon, which has indeed been reported for other bimetallic systems.[27,28]

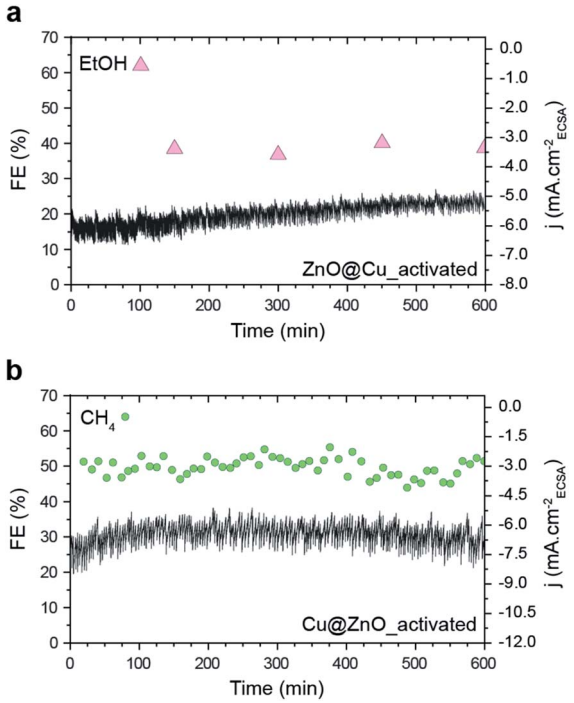

Fig. 5 Ethanol and methane FE and J_{total} of (a) activated ZnO@Cu at −1.3 V_{RHE} and (b) activated Cu@ZnO at −1.4 V_{RHE}. These potentials were selected as they result in the maximum FE for ethanol and methane, respectively.

CO_2RR measurements

The next step was to study the catalytic performance of the activated Cu@ZnO and ZnO@Cu toward the CO_2RR (Fig. 3, S9–S11†). Samples with a Zn atomic percentage equal to 54% were selected for further analysis as an initial electrocatalytic screening of the ZnO@Cu pre-catalysts indicated their higher selectivity towards ethanol (Fig. S10†). While a composition-dependent behavior was observed for the pre-catalysts with the same configuration, we found more intriguing the selectivity switch from ethanol to methane observed for activated ZnO@Cu and Cu@ZnO with the same composition. As discussed above, this observation is indeed highly relevant in the current state-of-the-art of CuZn systems.[9–15] Fig. 3 shows this difference in selectivity, which becomes particularly evident at potentials more negative than −1.1 V_{RHE}. The activated ZnO@Cu reaches a maximum faradaic efficiency (FE) for ethanol at −1.3 V *vs.* RHE, corresponding to 39%. Instead, the activated Cu@ZnO reaches a maximum FE for methane of 52% at −1.4 *vs.* RHE. This high methane selectivity was not observed in any of the ZnO@Cu samples with different Zn concentrations (Fig. S10†), which highlights the importance of the precatalyst configuration rather than simply altering the Cu/Zn ratio. Another interesting observation is that the FE for CO is always higher for the activated ZnO@Cu than for the activated Cu@ZnO across the entire potential range. It is also noteworthy that the total current density (J_{total} = $J_{CO2RR+HER}$) stays very similar for the two catalysts, along with a very similar electrochemically active surface area (ECSA, Fig. S9†).

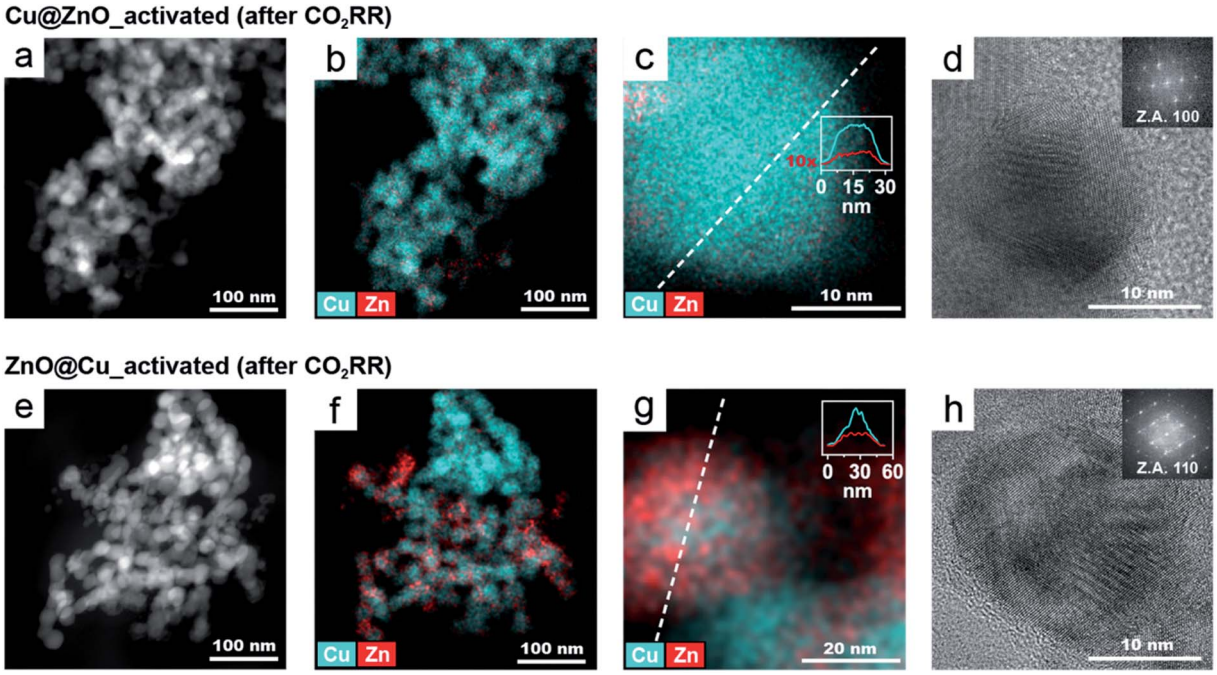

Fig. 6 HAADF-STEM image (a and e), EDX elemental maps (b, c, f, and g) and HRTEM images (d and h) of activated Cu@ZnO (a–d) and activated ZnO@Cu NCs (e–h), after the CO_2RR at -1.3 V_{RHE} for 2.5 hours. Insets in the high-resolution EDX maps show an intensity-weighted line profile along the dashed line. Insets in the HRTEM images show the corresponding FFTs used to assign the crystal structures (Z.A = zone axis).

To highlight the differences between the catalysts, Fig. 4 reports the FE_{EtOH}/FE_{CH_4} ratio and the partial current densities of EtOH, CH_4 and CO (J_{EtOH}, J_{CH_4} and J_{CO}). The FE_{EtOH}/FE_{CH4} ratio is higher on the activated ZnO@Cu at all of the studied potentials (Fig. 4a). The higher J_{EtOH} of the activated ZnO@Cu and the higher J_{CH_4} of the activated Cu@ZnO across the entire potential range confirm the higher intrinsic activity of the former toward the formation of EtOH and that of the latter toward the production of CH_4 (Fig. 4b and c). While J_{EtOH} plateaus at higher overpotentials (Fig. 4b), J_{CH_4} increases going toward more negative potentials (Fig. 4c). The observation that more cathodic potentials favour C_1 pathways over C–C coupling is in agreement with the literature and explains the decrease of the FE_{EtOH}/FE_{CH_4} ratio for both catalysts as the potential becomes more negative.[29–31]

It is interesting to note that the trend of J_{CO} as a function of potential is different for the two catalysts (Fig. 4d). The activity for CO production (indicated by J_{CO}) remains pretty much constant for the activated ZnO@Cu, and instead it decreases as the potential becomes more negative for the activated Cu@ZnO. Regarding the latter, it is expected that a higher portion of surface-bound CO species is likely to be reduced completely to methane rather than undergoing desorption or acting as a C_1 intermediate for C–C coupling.[31,32] The contrasting potential-independent activity for CO production (indicated by J_{CO}) in activated ZnO@Cu suggests that the ratio of active sites for supplying CO species in this sample is higher than that in Cu@ZnO. If this was not the case, we should have observed a drastic decrease in J_{CO}, since a huge fraction of surface-bound CO has to be consumed as an intermediate for CH_4 and EtOH production (see Fig. 4b and c). Nevertheless, the amount of residual CO that is desorbed in this sample remains unchanged.

It is worth noting that neither CH_4 nor EtOH is produced in significant amounts from activated ZnO, Cu and Cu–ZnO physical mixtures, which confirms once again the importance of the precatalyst configuration in this study (Fig. S11†). As for the stability, both activated ZnO@Cu and Cu@ZnO samples retain their FEs toward the production of EtOH and CH_4 for at least 10 hours (Fig. 5). This finding is opposite to other studies where the significant restructuring during the CO_2RR leads to performance changes.[15] As such, it highlights the importance of separating the structural changes of the catalysts during activation in order to achieve stable catalytic behavior.

Characterization of the CuZn catalysts during and after the CO_2RR

While the stability data do show the successful implementation of the activation step in achieving unchanged catalyst behaviour during operation, the different selectivities of the two catalysts still deserved further attention considering that they enter the course of the CO_2RR with no substantial structural or compositional difference. To obtain near-atomic level information, the samples were characterized by high-resolution TEM (HRTEM) and STEM-EDXS after the CO_2RR (Fig. 6). *Operando* XANES and extended X-ray absorption fine structure (EXAFS) measurements were also conducted on both catalysts (Fig. S12 and S13†). We selected -1.3 V_{RHE} for the detailed characterization as the difference in selectivity between the two catalysts was maximized at this potential.

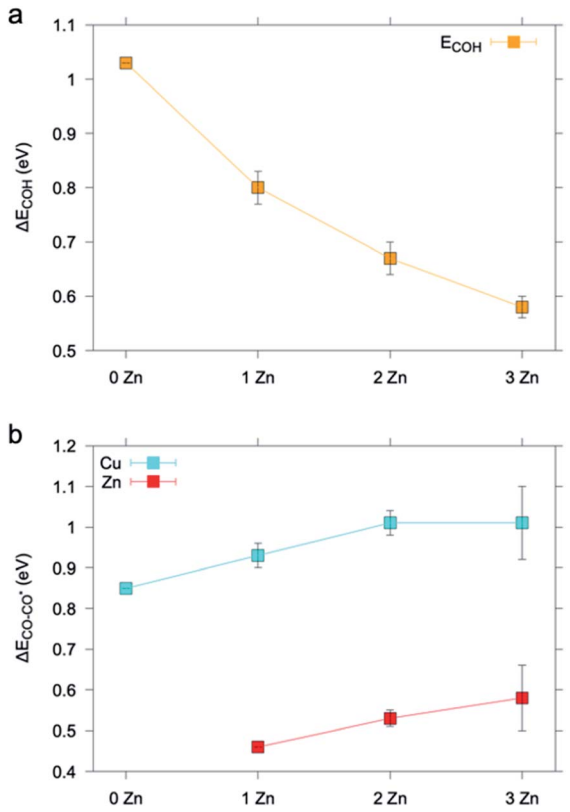

Fig. 7 (a) ΔE_{COH} and (b) ΔE_{CO-CO*} calculated on a pure Cu (111) slab embedding up to 3 Zn atoms. Results are averaged over data found for different non-equivalent adsorption sites (Fig. S18–S22†). The ΔE_{COH} value found for the Cu (111) slab matches that previously reported in the literature.[40] The ΔE_{CO-CO*} value found for the Cu (111) slab is in good agreement with that previously reported in the literature for CO adsorption and is an overestimate with respect to the experimental value.[43]

Fig. 6 shows the microscopy characterization of the catalysts post-CO_2RR. The low magnification STEM-EDXS maps of both activated NCs after the CO_2RR (Fig. 6a and e) evidence that their size and morphology remain stable during operation. However, the corresponding EDXS maps (Fig. 6b and f) show a lower amount of Zn in Cu@ZnO (5% Zn) compared to ZnO@Cu (19%) after the CO_2RR. These values were also confirmed by complementary inductively coupled plasma-optical emission spectrometry (ICP-OES) analysis on the catalysts post electrolysis.

The EDXS maps at higher magnification and the line profiles (Fig. 6c and g) shows that the Zn and Cu signals are colocalized in each NC. The distinct plateau in the middle of the Zn profile indicates that Zn is mostly present close to the catalyst surface and that the relative Zn amount decreases towards the centre of the particle.

The lattice spacing in the HRTEM images (Fig. 6d and h) corresponds to metallic Cu with a fcc crystal structure. No crystalline domains corresponding to Zn or ZnO were identified in any HRTEM images (nor in their corresponding FFT images). Overall, the electron microscopy characterization indicates that for both catalysts post-CO_2RR, the Zn atoms are dispersed at the surface. However, activated ZnO@Cu retains an almost 4-times higher concentration of Zn.

As for operando XAS, it should be noted that this technique provides information on the average NC structure. While during activation a very substantial reconstruction occurs, the changes during the CO_2RR are limited to the surface; therefore only subtle differences were observed (Fig. S12 and S13†). Nevertheless, the data were consistent with the presence of CuZn alloys in the shell of the activated catalysts with the degree of alloyed Cu in the ZnO@Cu-derived catalyst being qualitatively higher compared to that of the Cu@ZnO-derived catalyst.

Discussion of the general mechanism

To rationalize the interplay between the Zn content and location within NCs and the resulting catalyst selectivity, we performed density functional theory (DFT) simulations. A (111) surface slab, which is the lowest surface energy under vacuum, was chosen as a model of the Cu spherical domains.[33] We then studied the Zn impurity effect on the activity of Cu both as a function of its concentration and of its location. For the latter, we considered both the surface and subsurface as a preference of the Zn atoms to segregate and islanding in either location was not found (Fig. S14†).[34]

First, we found that the presence of one or more Zn atoms modifies the electronic structure of the system with respect to the case of a pure Cu surface (Fig. S15–S19†). Bader charge analysis[35,36] shows a mean charge transfer of 0.15 e^- from each Zn atom in the system. On average, the d-band center for Cu adsorption sites[37,38] is downshifted with respect to the bare Cu surface by 0.4, 0.35, and 0.26 eV in the presence of one, two, or three Zn atoms. The same parameter evaluated at Zn adsorption sites is slightly upshifted.

We then moved to evaluate the impact of Zn on the energetics of the CO_2 reduction pathway. As COH was a crucial intermediate towards CH_4, we chose the formation energy of COH from adsorbed CO, ΔE_{COH}, as the activity descriptor and utilized the computational hydrogen electrode model to evaluate the energetics of the elementary proton transfer step (see also the ESI†).[39,40] We considered only Cu sites as the catalytically active ones because Cu is the only metal known to form CO_2RR products beyond CO.[41,42] As illustrated in Fig. 7a and S15–S16,† the ΔE_{COH} value decreases as soon as one Zn atom is introduced into the copper slab and it changes to a lesser extent as the number of Zn atoms increases or their location (*i.e.* surface or subsurface) changes.

To rationalize the higher CO production of the activated ZnO@Cu NCs, we considered the change of CO desorption energy, ΔE_{CO-CO*},[43] at the Cu and Zn sites as Zn atoms are added into Cu. Fig. 7b and S17–S19† show that ΔE_{CO-CO*} increases on both the Cu site and the Zn site as one to a few Zn atoms are added into the system. In agreement with d-band theory,[37,38] the Zn adsorption site d-band upshift corresponds to a stronger metal-adsorbate interaction. *Vice versa*, the trends found for the case of Cu represent an exception to predictions drawn from d-band theory.[44] This behavior has been already previously reported in other theoretical studies on the adsorption properties

of Cu sites in CuZn systems.[45] We note that future and dedicated studies may be conducted to clarify the origin of this exception.

The increase in the strength with which CO is adsorbed on the Cu sites is beneficial to the selective reduction of CO_2 to C^{2+} products.[31] On the other hand, the absolute value of ΔE_{CO-CO^*} is lower for the Zn site, consistent with Zn being a CO-producing metal.[41,46] This finding implies that the higher the Zn concentration is, the more the CO evolution is favored, which is also related to the increased possibility that Zn atoms cluster on the surface. Having learned this, we speculate that the increase in EtOH production for the activated ZnO@Cu NCs is further connected to tandem effects, which is consistent with previous observations.[10,43] Notice that oxophilicity, *i.e.* the ability of secondary components to increase the formation of oxygenates, has also been proposed, and actually, the binding energy of O atoms to Zn is larger than that of Cu alone.[47] Our computational results are in line with the experimental observations demonstrating higher alcohol formation for the samples containing more Zn on the surface of ZnO@Cu. In addition, it demonstrates how robust structure–activity relationships require the exquisite characterization of the fine details of the structure and how composition only analyses are a too simplified proxy for the structure.

Conclusions

In summary, this work has introduced tailored Cu/ZnO NCs as precatalysts for the CO_2RR to investigate the compositional and structural sensitivities of the CO_2RR in bimetallic Cu–Zn catalysts. We found that Cu@ZnO and ZnO@Cu NCs evolve towards alloyed CuZn in a core@shell configuration, with a Cu-rich core and a Zn-rich shell. The ZnO@Cu-derived and Cu@ZnO-derived catalysts showed selectivity for ethanol and methane, respectively. The main difference between the two stems from the higher degree of surface alloying and higher concentration of metallic Zn in the EtOH selective catalyst.

DFT simulations show that diluted amounts of Zn impurities affect the electronic structure of the catalyst and promote CH_4 selectivity, while a higher Zn content increases the local CO concentration and enables a tandem conversion mechanism which determines the selectivity shift from CH_4 to EtOH.

This conclusion helps to reconciliate previous results in the literature. In particular, a lower degree of alloying promotes the formation of CH_4 is consistent with the results reported by Jeon *et al.*, who investigated Cu–Zn nano catalysts in a similar size regime and composition.[15] The higher degree of surface alloying is in line with another study, where CuZn bimetallic catalysts obtained by *in situ* electrochemical reduction of CuO and ZnO promoted the selectivity towards EtOH, in which case a tandem catalysis mechanism was proposed.[10] In addition, the present results indicate that composition is not a single descriptor for activity and that the local structure is crucial to performance. Indeed, we provide evidence that materials with identical compositions evolve into different catalysts even under strong catalytic equilibration conditions.

Towards the future, synergies between tandem and electronic effects are to be sought after to rationally tune bimetallic catalyst selectivity towards desired products, such as alcohols. In this direction, studies on Cu@ZnO core@shell synthesized *via* colloidal ALD are envisioned to achieved atomic control and will help to investigate further this topic.[48]

Experimental section

Chemicals

Copper(I) acetate (or Cu(OAc), 97%), trioctylphosphine ($\{CH_3(CH_2)_7\}_3P$, or TOP, 90%), oleic acid ($C_{17}H_{33}CO_2H$ or OLAC, 90%), oleylamine ($C_{17}H_{33}NH_2$ or OLAM, 70%), and 1-octadecene ($C_{18}H_{36}$ or ODE, 90%) were all purchased from Sigma Aldrich and used as received.

Synthesis of Cu/ZnO precatalysts

30 mL of an ODE solution containing pre-synthesized ZnO NCs (0.5 mM) in a 100 mL three-necked flask were degassed under dynamic vacuum for 20 min at 130 °C, after which they were heated under a N_2 flow to 300 °C for 5 minutes. ZnO NCs of 13 nm or 60 nm were used as nucleation seeds for the copper (Fig. S1†). The copper precursor solution was prepared by mixing 0.1 mmol of Cu(OAc), 0.396 mmol of TOP, 0.02 mmol of OLAM and 0.02 mmol of OLAC in degassed ODE (1.4 mL). To obtain a Zn atomic percentage of 54%, 450 μL of this solution were then added dropwise to the flask containing the seeds at a rate of 0.18 mL min^{-1} using a syringe pump, during which the colour of the reaction mixture slowly changed from colourless to brown. At the end of the injection, after around 150 s, the reaction was stopped, and the mixture was allowed to cool down to room temperature by removing the heating mantle. The NCs were extracted and purified by repeated washing/centrifugation cycles inside a N_2 glovebox to avoid Cu oxidation. 30 mL each of anhydrous EtOH and toluene were added to the reaction mixture at room temperature and the mixture was divided into four centrifugation vials; the particles were collected by centrifugation at 5000 rpm for 15 min. The precipitate was washed twice with EtOH to remove unreacted precursor and surfactants. Finally, the NCs were re-dispersed in hexane or toluene for storage.

Characterization

Electron microscopy. Samples were drop-cast on a transmission electron microscopy (TEM) grid (Ted Pella, Inc.) prior to imaging. Bright field TEM images were taken with a FEI Tecnai Spirit at 120 keV. Scanning transmission electron microscopy and high angle annular dark field imaging (STEM-HAADF) as well as energy dispersive X-ray spectroscopy (EDXS) were performed on a FEI Tecnai Osiris transmission electron microscope in scanning mode at an accelerating voltage of 200 kV. This microscope is equipped with a high brightness X-FEG gun, silicon drift Super-X EDXS detectors and a Bruker Esprit acquisition software. Aberration-corrected high-resolution TEM (HRTEM) and STEM-HAADF data were acquired

using a Thermo Fisher Scientific Titan Themis operated at 300 kV with dual aberration correctors.

X-ray photoelectron spectroscopy (XPS). XPS was carried out using an Axis Supra (Kratos Analytical) instrument. Analysis was carried out using a monochromatic Al Kα X-ray source operating at 25 W with a beam size of 100 μm. The pass energy was set to 20 eV with a step size of 0.1 eV. Samples were measured on clean Si wafers, electrically insulated from the sample holder and charges were compensated. The binding energy of the spectra was calibrated by setting the C–C bond of the C 1s peak at 284.8 eV.

Inductively coupled plasma-optical emission spectrometry (ICP-OES). ICP-OES was performed on an Agilent 5100 set-up to determine the elemental concentrations. Metal ions were digested after the evaporation of the hexane/toluene solvent (100 μL of the stock solution was used per analysis). 285 μL of HNO_3 (70%) was added to the nanocrystals (NCs) and left overnight to ensure complete digestion of the samples. Following this step, 9.715 mL of Milli-Q water was added to the solution to reach the 2% acid content needed for the analysis. 5 standard solutions of each element were prepared to obtain the calibration curve that was used to determine the concentrations of the digested solutions.

X-ray diffraction (XRD). XRD was carried out on a Bruker D8 Advance diffractometer with a Cu Kα source equipped with a Lynxeye one-dimensional detector. The diffractometer was operated at 40 kV and 40 mA with a Cu Kα source with a wavelength of $\lambda = 1.54$ Å.

Thermogravimetric analysis (TGA). In order to determine the loading of metal oxide NC seeds, 60 μL of the NC stock solution was deposited in an aluminium pan, and the solvent was evaporated. The pan was then introduced into a TGA Q500 with an air flow rate of 15 mL min^{-1}. The sample was heated to 600 °C with a heating ramp of 10 °C min^{-1}. On the basis of the final weight, the concentrations of metal oxide solutions were calculated.

Electrocatalytic measurements

Electrochemical CO_2RR. The electrocatalytic testing was performed in a custom-made electrochemical flow cell. Glassy carbon plate electrodes (Type 2, Alfa Aesar) with a surface area of 2.5 cm × 2.5 cm were used as substrates. They were polished using Milli-Q water slurries of 1 μm diamond (Bioanalytical Systems, Inc.) and 50 nm γ-alumina (Bioanalytical Systems, Inc.) on polishing pads. The plates were rinsed and sonicated in Milli-Q water for 10 min and blown dry with nitrogen. The NC samples were drop-cast on the substrate from toluene suspensions, giving a mass loading of 15 μg. Electrochemical measurements were carried out using a Biologic SP-300 potentiostat. Platinum foil was employed as the counter electrode, and an Ag/AgCl reference electrode (leak free series from Innovative Instruments, Inc.) was used. Voltages were converted to the reversible hydrogen electrode (RHE) scale. Ambient-pressure CO_2 electrolysis was performed in a custom-made gastight electrochemical cell made of poly(methyl methacrylate) and fitted with Buna-N O-rings. The configuration of the electrochemical cell was such that the working electrode sat parallel with respect to the counter electrode to ensure a uniform potential distribution across the surface. The geometric surface area of both electrodes was 1 cm^2. Each of the compartments in this cell was filled with the electrolyte (CO_2 saturated 0.1 M $KHCO_3$ solution, 2.1 mL in each half). A Selemion AMV anion-exchange membrane was used to separate the anodic and cathodic compartments. The electrolyte solution was prepared by sparging a 0.05 M K_2CO_3 solution with CO_2 for 1 h. Before CO_2 electrolysis, the electrolyte in the cell was sparged with CO_2 for at least 15 min. During electrolysis, CO_2 was constantly bubbled through the electrolyte at a flow rate of 5 sccm to prevent the depletion of CO_2 in the electrolyte and to enable continuous analysis of gaseous products using a gas chromatograph. The flow rate of CO_2 was controlled with a mass flow-controller (Bronkhorst), and the gas was first humidified with water by passing it through a bubbler to minimize the evaporation of the electrolyte. The calibration of the gas chromatograph was done using calibration gas standards from Carbogen. CO, CH_4, C_2H_4 and C_2H_6 were all calibrated from calibration mixtures at five different concentrations: 50, 100, 250, 500, and 1000 ppm. H_2 was likewise calibrated using 500, 1000, 5000, and 10 000 ppm of H_2 balanced in nitrogen. After passing through the cell, CO_2 was flowed directly into the gas-sampling loop of the GC for online gaseous product analysis, which was carried out every 10 min. The chronoamperometry experiments were performed for a total of 2.5 hours. The liquid products were collected from the electrolyte after electrolysis and analysed by high-performance liquid chromatography (HPLC) on an UltiMate 3000 instrument from Thermo Scientific.

Operando X-ray absorption spectroscopy (XAS)

Operando. XAS experiments were performed at the Swiss-Norwegian beamlines BM31 at the European Synchrotron Radiation Facility (ESRF) in France. The catalyst solution was drop-casted on a thin (2.5 × 2.5 × 0.5 mm^3) glassy carbon (GC) support and a Kapton window allowed the X-rays to pass through. For standards and other *ex situ* measurements (typically in the pellet form and with the catalyst diluted in a light matrix such as boron nitride or cellulose to obtain an appropriate thickness, typically of 2–3 absorption lengths), we used a traditional system based on ionization chambers for transmission detection.

The measurements were carried out in fluorescence mode at an incident angle of approximately 45 degrees. A Si(111) double crystal monochromator (DCM) was used to condition the beam from the corresponding bending magnet. Fluorescence X-ray absorption near edge structure (XANES) spectra were acquired using a Vortex® one-element silicon drift detector (SDD) with XIA-Mercury digital electronics with a time-resolution of 1 min per spectrum at both Cu and Zn K-edges (*i.e.* 2 min per Cu/Zn cycle). Data extraction, normalization, and averaging were performed using the beamline dedicated software for QEXAFS data analysis, PrestoPronto.[17]

The Demeter package (Athena and Artemis)[18] was employed for the EXAFS fitting of the catalyst. Finally, a multi-use beamline fixation support permits the cell alignment with respect to the incoming beam *via* an XYZ high-precision translation stage.

Multivariate curve resolution (MCR) analysis. We have made use of multivariate curve resolution using an alternating least-square mathematical algorithm (MCR-ALS) to analyse the large number of XANES spectra generated during the *operando* CO_2RR measurements. MCR-ALS is a data-reduction tool that can extract (even in a blind manner) kinetically pure component spectra and the corresponding concentration profiles out of an unresolved mixture.[19–21] The MCR-ALS model relies on the $D = CS^T + E$ mathematical equation, where D: initial matrix composed of all collected spectra, C: extracted concentration profiles, S: extracted spectra profiles (T stands for the transposed matrix), and E: error matrix containing the residuals and close to the experimental error. The MCR-ALS graphical user interface (GUI) for MATLAB used in this paper (freeware available at http://www.mcrals.info/) was applied on the Cu and Zn K-edge time-resolved datasets by employing positive constraints for both spectra and concentration profiles, and closure constraints for the concentration profiles (*i.e.* constant concentration of the absorbing atoms throughout the experiment).

Density functional theory calculations

Density Functional Theory (DFT) calculations were carried out with CP2K software.[22] A DZVP-MOLOPT[23] basis set was used in the calculations, with core electrons being described with dual-space Goedecker–Teter–Hutter[24] pseudopotentials. The plane waves and relative cut-off were set to 500 Ry and 50 Ry respectively. For adsorption energy calculations, the (111) Cu facet was chosen, in agreement with the observed orientation found in XRD. A (4×4) slab with 4 layers was considered. Replicas along the axis normal to the (111) slabs are separated by 22 Å. Surface dipole corrections were applied along the plane normal to the surface. The two bottom layers of the surface were kept fixed during structural relaxations. The latter were deemed converged when all the atomic forces were found to be at least less than 0.009 H per Bohr ($\sim$0.45 meV A^{-1}). The DFT calculations of the energy of the system were instead converged when a change less than 10^{-6} H was registered between two successive self-consistent electronic density calculation loops.

Data availability

The most relevant inputs and outputs of the DFT calculations are available on the Materials Cloud, DOI: 10.24435/materialscloud:3r-gn.

Author contributions

S. B. V. and R. B. conceived and designed the experiments. S. B. V. carried out the chemical synthesis and the electrochemical experiments and analysed the results. S. B. V. and D. S. performed the XAS experiments. D. S. analyzed the XAS results. S. B. V. and J. V. performed the electron microscopy characterization. K. R. and N. L. developed the methodology and performed the DFT calculations. J. R. P. carried out and analyzed the XPS measurements. Y. T. G. contributed to the HPLC measurements. S. B. V. and R. B. assembled the figures and co-wrote the manuscript. All authors discussed the results and commented on the manuscript.

Conflicts of interest

There are no conflicts to declare.

Acknowledgements

This work was financially supported by the European Research Council (ERC) under the European Union's Horizon 2020 research and innovation program (grant agreement no. 715634-HYCAT). JRP and KR acknowledge the H2020 Marie Curie Individual Fellowship grants SURFCAT and NANOCO2RE with agreement numbers 837378 and 890414, respectively. D. S. was supported by the Sandoz Foundation. The theoretical effort was supported by EPFL computational facilities and the Swiss National Supercomputer Center (CSCS), project "sm54". We thank Dr F. Dattila for useful discussions regarding the technical aspects of the simulations. This publication was created as part of NCCR Catalysis, a National Centre of Competence in Research funded by the Swiss National Science Foundation.

Notes and references

1 S. Nitopi, E. Bertheussen, S. B. Scott, X. Liu, A. K. Engstfeld, S. Horch, B. Seger, I. E. L. Stephens, K. Chan, C. Hahn, J. K. Nørskov, T. F. Jaramillo and I. Chorkendorff, *Chem. Rev.*, 2019, **119**, 7610–7672.
2 D. Karapinar, C. E. Creissen, J. G. Rivera De La Cruz, M. W. Schreiber and M. Fontecave, *ACS Energy Lett.*, 2021, **6**, 694–706.
3 F. Li, Y. C. Li, Z. Wang, J. Li, D. H. Nam, Y. Lum, M. Luo, X. Wang, A. Ozden, S. F. Hung, B. Chen, Y. Wang, J. Wicks, Y. Xu, Y. Li, C. M. Gabardo, C. T. Dinh, Y. Wang, T. T. Zhuang, D. Sinton and E. H. Sargent, *Nat. Catal.*, 2020, **3**, 75–82.
4 C. G. Morales-Guio, E. R. Cave, S. A. Nitopi, J. T. Feaster, L. Wang, K. P. Kuhl, A. Jackson, N. C. Johnson, D. N. Abram, T. Hatsukade, C. Hahn and T. F. Jaramillo, *Nat. Catal.*, 2018, **1**, 764–771.
5 L. R. L. Ting, O. Piqué, S. Y. Lim, M. Tanhaei, F. Calle-Vallejo and B. S. Yeo, *ACS Catal.*, 2020, **10**, 4059–4069.
6 P. Iyengar, M. J. Kolb, J. R. Pankhurst, F. Calle-Vallejo and R. Buonsanti, *ACS Catal.*, 2021, **11**, 4456–4463.
7 S. Lee, G. Park and J. Lee, *ACS Catal.*, 2017, **7**, 8594–8604.
8 Y. C. Li, Z. Wang, T. Yuan, D. H. Nam, M. Luo, J. Wicks, B. Chen, J. Li, F. Li, F. P. G. De Arquer, Y. Wang, C. T. Dinh, O. Voznyy, D. Sinton and E. H. Sargent, *J. Am. Chem. Soc.*, 2019, **141**, 8584–8591.
9 D. Ren, B. S. H. Ang and B. S. Yeo, *ACS Catal.*, 2016, **6**, 8239–8247.

10 D. Ren, J. Gao, L. Pan, Z. Wang, J. Luo, S. M. Zakeeruddin, A. Hagfeldt and M. Grätzel, *Angew. Chemie Int. Ed.*, 2019, **58**, 15036–15040.
11 Z. Li, R. M. Yadav, L. Sun, T. Zhang, J. Zhang, P. M. Ajayan and J. Wu, *Appl. Catal., A*, 2020, **606**, 117829.
12 A. H. M. da Silva, S. J. Raaijaman, C. S. Santana, J. M. Assaf, J. F. Gomes and M. T. M. Koper, *J. Electroanal. Chem.*, 2020, **880**, 114750.
13 H. Hu, Y. Tang, Q. Hu, P. Wan, L. Dai and X. J. Yang, *Appl. Surf. Sci.*, 2018, **445**, 281–286.
14 G. Keerthiga and R. Chetty, *J. Electrochem. Soc.*, 2017, **164**, H164–H169.
15 H. S. Jeon, J. Timosnenko, F. Scholten, I. Sinev, A. Herzog, F. T. Haase and B. R. Cuenya, *J. Am. Chem. Soc.*, 2020, **141**, 19879–19887.
16 L. Wang, H. Peng, S. Lamaison, Z. Qi, D. M. Koshy, M. B. Stevens, D. Wakerley, J. A. Zamora Zeledón, L. A. King, L. Zhou, Y. Lai, M. Fontecave, J. Gregoire, F. Abild-Pedersen, T. F. Jaramillo and C. Hahn, *Chem. Catal.*, 2021, **1**, 663–680.
17 S. J. A. Figueroa and C. Prestipino, in *Journal of Physics: Conference Series*, Institute of Physics Publishing, 2016, vol. 712, 1–4, p. 012012.
18 B. Ravel and M. Newville, *J. Synchrotron Radiat.*, 2005, **12**, 537–541.
19 C. Ruckebusch and L. Blanchet, *Anal. Chim. Acta*, 2013, **765**, 28–36.
20 A. De Juan, J. Jaumot and R. Tauler, *Anal. Methods*, 2014, **6**, 4964–4976.
21 J. Jaumot, R. Gargallo, A. De Juan and R. Tauler, *Chemom. Intell. Lab. Syst.*, 2005, **76**, 101–110.
22 J. Hutter, M. Iannuzzi, F. Schiffmann and J. Vandevondele, *Wiley Interdiscip. Rev.: Comput. Mol. Sci.*, 2014, **4**, 15–25.
23 J. VandeVondele and J. Hutter, *J. Chem. Phys.*, 2007, **127**, 114105.
24 M. Krack, *Theor. Chem. Acc.*, 2005, **114**, 145–152.
25 S. B. Varandili, J. Huang, E. Oveisi, G. L. De Gregorio, M. Mensi, M. Strach, J. Vavra, C. Gadiyar, A. Bhowmik and R. Buonsanti, *ACS Catal.*, 2019, **9**, 5035–5046.
26 S. B. Varandili, D. Stoian, J. Vavra, J. Pankhurst and R. Buonsanti, *Chem. Sci.*, 2020, **11**, 13094–13101.
27 M. Gatalo, P. Jovanovič, U. Petek, M. Šala, V. S. Šelih, F. Ruiz-Zepeda, M. Bele, N. Hodnik and M. Gaberšček, *ACS Appl. Energy Mater.*, 2019, **2**, 3131–3141.
28 M. Gatalo, P. Jovanovič, F. Ruiz-Zepeda, A. Pavlišič, A. Robba, M. Bele, G. Dražić, M. Gaberšček and N. Hodnik, *J. Electrochem. Sci. Eng.*, 2018, **8**, 87–100.
29 T. K. Todorova, M. W. Schreiber and M. Fontecave, *ACS Catal.*, 2020, **10**, 1754–1768.
30 I. Ledezma-Yanez, E. P. Gallent, M. T. M. Koper and F. Calle-Vallejo, *Catal. Today*, 2016, **262**, 90–94.
31 K. P. Kuhl, E. R. Cave, D. N. Abram and T. F. Jaramillo, *Energy Environ. Sci.*, 2012, **5**, 7050.
32 L. Ou and J. Chen, *Phys. Chem. Chem. Phys.*, 2019, **22**, 62–73.
33 R. Tran, Z. Xu, B. Radhakrishnan, D. Winston, W. Sun, K. A. Persson and S. P. Ong, *Sci. Data*, 2016, **3**, 1–13.
34 N. López and C. Vargas-Fuentes, *Chem. Commun.*, 2012, **48**, 1379–1391.
35 G. Henkelman, A. Arnaldsson and H. Jónsson, *Comput. Mater. Sci.*, 2006, **36**, 354–360.
36 R. F. W. Bader, *Chem. Rev.*, 2002, **91**, 893–928.
37 B. Hammer and J. K. Norskov, *Nature*, 1995, **376**, 238–240.
38 A. Vojvodic, J. K. Nørskov and F. Abild-Pedersen, *Top. Catal.*, 2014, **57**, 25–32.
39 J. K. Nørskov, J. Rossmeisl, A. Logadottir, L. Lindqvist, J. R. Kitchin, T. Bligaard and H. Jónsson, *J. Phys. Chem. B*, 2004, **108**, 17886–17892.
40 Z. Wang, Q. Yuan, J. Shan, Z. Jiang, P. Xu, Y. Hu, J. Zhou, L. Wu, Z. Niu, J. Sun, T. Cheng and W. A. Goddard, *J. Phys. Chem. Lett.*, 2020, **11**, 7261–7266.
41 X. Liu, J. Xiao, H. Peng, X. Hong, K. Chan and J. K. Nørskov, *Nat. Commun.*, 2017, **8**, 1–7.
42 A. Bagger, W. Ju, A. S. Varela, P. Strasser and J. Rossmeisl, *ChemPhysChem*, 2017, **18**, 3266–3273.
43 Y. Huang, Y. Chen, T. Cheng, L. W. Wang and W. A. Goddard, *ACS Energy Lett.*, 2018, **3**, 2983–2988.
44 H. Xin and S. Linic, *J. Chem. Phys.*, 2010, **132**(1–4), 221101.
45 X. Fan, Q. L. Tang, X. Zhang, T. T. Zhang, Q. Wang, X. X. Duan, M. L. Zhang and M. Y. Yao, *Appl. Surf. Sci.*, 2019, **469**, 841–853.
46 Y. Hori, in *Modern Aspects of Electrochemistry*, Springer, New York, 2008, pp. 89–189.
47 L. R. L. Ting, R. García-Muelas, A. J. Martín, F. L. P. Veenstra, S. T.-J. Chen, Y. Peng, E. Y. X. Per, S. Pablo-García, N. López, J. Pérez-Ramírez and B. S. Yeo, *Angew. Chem.*, 2020, **132**, 21258–21265.
48 A. Loiudice, M. Strach, S. Saris, D. Chernyshov and R. Buonsanti, *J. Am. Chem. Soc.*, 2019, **141**, 8254–8263.